

Application of the sparse-Lagrangian multiple mapping conditioning approach to a model supersonic combustor

Cite as: Phys. Fluids **32**, 105120 (2020); <https://doi.org/10.1063/5.0026654>

Submitted: 25 August 2020 . Accepted: 06 October 2020 . Published Online: 21 October 2020

Zhiwei Huang (黄志伟) , Matthew J. Cleary , and Huangwei Zhang (张黄伟) 



View Online



Export Citation



CrossMark

Physics of Fluids
Special Issue on the **Lattice Boltzmann Method**

SUBMIT TODAY!



Application of the sparse-Lagrangian multiple mapping conditioning approach to a model supersonic combustor

Cite as: Phys. Fluids 32, 105120 (2020); doi: 10.1063/5.0026654

Submitted: 25 August 2020 • Accepted: 6 October 2020 •

Published Online: 21 October 2020



View Online



Export Citation



CrossMark

Zhiwei Huang (黄志伟),¹  Matthew J. Cleary,²  and Huangwei Zhang (张黄伟)^{1,a)} 

AFFILIATIONS

¹Department of Mechanical Engineering, National University of Singapore, 9 Engineering Drive 1, Singapore 117576, Republic of Singapore

²School of Aerospace, Mechanical and Mechatronic Engineering, The University of Sydney, New South Wales 2006, Australia

^{a)}Author to whom correspondence should be addressed: huangwei.zhang@nus.edu.sg. Tel.: +65 6516 2557

ABSTRACT

The Multiple Mapping Conditioning/Large Eddy Simulation (MMC-LES) model is extended for the first time to high-speed, compressible flow conditions and validated against non-reacting and reacting experimental data from a model supersonic combustor. The MMC-LES method solves the subgrid joint composition filtered density function through a Monte Carlo approach, and it permits a low-cost numerical implementation using a sparse distribution of stochastic Lagrangian particles. The sensitivity of results to the particle resolution is examined, and similar to past low-speed applications of MMC-LES, that sensitivity is found to be low. In comparison to the model equations for subsonic turbulent combustion conditions, the pressure work and viscous heating effects have been incorporated here to account for the effects of compressibility. As expected, the viscous heating effects are small for this flow case and can be ignored, while the pressure work is not negligible and makes a significant contribution at expansion fans and shock fronts where the magnitude of the pressure derivative term in non-reacting/reacting cases is as much as 23.8%/24.5% and 19.2%/18.6% of the stochastic particle standardized enthalpy, respectively. The MMC-LES predictions show good quantitative agreement with the available experimental data for the mean and root-mean-square of axial velocity, mean temperature, and wall pressure. Good qualitative comparison to the data is also observed for major flow characteristics, including location and size of shocks, expansion fans, and recirculation zone, and combustion characteristics such as flame lift-off distance. Although the effects of the pressure work on the mean flame lift-off distance are negligible, they have a significant influence on the predicted spatial fluctuations of the flame base.

Published under license by AIP Publishing. <https://doi.org/10.1063/5.0026654>

I. INTRODUCTION

Fuel mixing and combustion in supersonic flows are key scientific problems in developing high-speed propulsion systems.¹ They have been extensively investigated through both experimental and numerical methods in recent years.^{2,3} In particular, Large Eddy Simulation (LES) can provide detailed insights into turbulent supersonic combustion physics at an increasingly affordable computational cost, and hence, it is now widely used for modeling fundamental and applied flows and combustion configurations, including coflow jet flames,^{4,5} crossflow jet flames,^{6–8} and model combustors.^{9,10} Due to the high Mach and Reynolds numbers, supersonic combustion

generally proceeds in highly turbulent flows with strong fluctuations of reactive scalars and flow discontinuities (e.g., shock waves). Accurate simulation requires sophisticated and realizable closure models, particularly for the highly non-linear reaction rates, although there are still some studies without models, e.g., for supersonic¹¹ and detonative^{12,13} combustion.

The quasi-laminar chemistry method, which explicitly neglects the effects of subgrid reactive scalar fluctuations and directly computes only the resolved reaction rates, is commonly used in simulations of high-speed reacting flows.³ Strictly speaking, the method is valid only when the subgrid turbulent mixing time scales are much smaller than the chemical time scales.¹⁴ This condition holds only

if the LES is well resolved (hence expensive), especially for simulations of flames that manifest strong unsteadiness due to turbulence–chemistry interactions (TCIs), such as ignition and extinction, and flame–shock interactions. Jaber *et al.*¹⁵ quantitatively demonstrated the errors associated with neglecting the subgrid reaction rates. In that work, it was found that the quasi-laminar chemistry model drastically over-predicted the rate of product formation. Accurate and affordable LES of supersonic combustion, therefore, requires the use of advanced sub-grid scale combustion models that have, so far, seen much wider applications in subsonic combustion applications.

Two common classes of probabilistic TCI models are (i) the flamelet-like models¹⁶ [including the conditional moment closure (CMC)¹⁷], which parameterize the composition in terms of conditioning or manifold parameters and use a presumed form probability density function (PDF) for the subgrid fluctuations of those parameters; and (ii) the transported PDF models,¹⁸ which solve transport equations for the unresolved distributions. In the context of LES, solutions are obtained for the filtered density function (FDF),¹⁵ and this is the terminology used in the present work. The flamelet-like models are relatively computationally economical but are formally limited to specific flame regimes determined by the chosen conditioning parameters. In the context of subsonic flows, the flamelet-like models have been widely developed for the non-premixed regime,^{19–21} and there is now an increasing application to the premixed regime as well.^{22–24} They have also been successfully applied for two-phase combustion modeling (e.g., coal²⁵ and spray²⁶ combustion) and supersonic combustion modeling, e.g., in the work of Saghafian *et al.*,⁶ Ladeinde *et al.*,²⁷ and Picciani.²⁸ PDF methods are more general and mathematically accurate in terms of closing the TCIs because the non-linear chemical source terms are naturally closed independent of the specific turbulence model or any specific flame regime.¹⁸ However, PDF/FDF methods also have challenges, particularly surrounding the difficulty in finding a universal model for the subgrid scale (micro)mixing, and their high dimensionality that can lead to a large computational cost.^{29,30} The latter is exacerbated for practical hydrocarbon fuels whose chemical kinetics are stiff and may involve hundreds of species.³¹ The most economical solution method, but still relatively expensive compared to flamelet models, involves recasting the continuum PDF/FDF transport equations in stochastic form that is readily solved in a Monte Carlo simulation using an ensemble of Lagrangian particles.¹⁸ The application of PDF models to supersonic flames can be found in the work of Zhang *et al.*³² and De Almeida and Navarro-Martinez.³³

The Multiple Mapping Conditioning (MMC) approach^{34,35} aims to tackle both the mixing model and cost challenges of PDF methods. In its stochastic form, MMC is a full transported PDF/FDF method that also introduces the aspects of the flamelet-like models through a mixing model that preserves conditional mean scalar values by localization of that mixing in composition space. Mixing localness in composition space is a vital property of PDF mixing models,³⁶ which is done indirectly in MMC by localizing the mixing in a mathematically independent reference space that is correlated with the composition. Use of the reference space ensures that two other vital mixing model properties, namely, independence and linearity of mixing,³⁶ are preserved for all scalars. In LES of non-premixed flames, the filtered mixture fraction solved in an Eulerian

fashion on the LES grid is an appropriate reference variable since it effectively parameterizes the composition while also being mathematically independent of the composition field on the stochastic Lagrangian particles.³⁵ In MMC-LES, the enforced localness in Reference Mixture Fraction (RMF) space permits a relaxation of strict mixing localness in physical space and a reduction in the number of Lagrangian particles compared to approaches with conventional (non-local) mixing models. The so-called sparse-Lagrangian MMC-LES involves significantly fewer particles for the stochastic composition field than the Eulerian grid cells for the LES flow solution. Thus, the computational cost is significantly lower than the conventional FDF methods with an intensive distribution of particles. Sparse MMC-LES has been extensively validated for a range of low-Mach experimental combustion configurations of practical relevance, e.g., piloted methane/air jet diffusion flames,³⁷ methane/air swirl flames,³⁸ the Sandia DME flame series,³⁹ and turbulent spray flames.⁴⁰ The numerical convergence of sparse MMC-LES has been demonstrated over a three-order magnitude variation in stochastic particle number in the direct numerical simulation (DNS) study by Vo *et al.*,⁴¹ while other studies of experimental jet flames have also shown a low sensitivity to the particle number.^{38,42}

The objective of this work is to extend the MMC-LES model to supersonic flows for the first time with quantitative and qualitative validation against the experimental data for a model combustor.⁴³ The previously applied low-Mach version of the model omits pressure work and viscous heating terms in the transport equations, and these are added here and their influences on the predictions of the thermo-chemical structures and the unsteady supersonic flame behavior are studied. Additionally, the numerical scheme in our open source *mmcFoam* code⁴² is upgraded to permit discontinuities at shocks without inducing numerical instability. Hence, the novelty of this work lies in two aspects. First, the present model incorporates a sophisticated closure for combustion including subgrid fluctuations but with fewer particles required than the LES cells for evaluation of the composition. Second, the present work incorporates and evaluates the importance of compressibility terms in supersonic flows and concludes that the pressure work term, in particular, is important. The rest of this paper is organized as follows: The compressible MMC-LES formulations and implementation into the *mmcFoam* solver are detailed in Sec. II, while the case configuration and computational setup are presented in Sec. III. The results and discussion are found in Sec. IV, followed by the conclusion in Sec. V.

II. GOVERNING EQUATIONS AND NUMERICAL IMPLEMENTATION

MMC-LES is a hybrid approach where the filtered equations for mass, momentum, and reference mixture fraction are solved using Eulerian LES, while the Stochastic Differential Equations (SDEs) are solved on an ensemble of Lagrangian notional particles for the joint FDF of species mass fractions and standardized enthalpy (i.e., enthalpy of formation plus sensible enthalpy). This choice of FDF state space leads to the neglect of the direct effects of subgrid pressure fluctuations on the composition and requires some discussion. De Almeida and Navarro-Martinez³³ recently validated the Eulerian stochastic field implementation of the FDF model against the data for a supersonic lifted flame. Two versions of the model,

with different FDF state spaces, were tested. In the first version, the FDF state space includes species mass fractions and enthalpy, which is conventional for FDF methods. The FDF chemical source terms are calculated using the filtered pressure, and although that filtered pressure incorporates the effects of subgrid fluctuations of composition and temperature through the ideal gas equation of state, the direct effects of subgrid pressure fluctuations on the reaction rates are neglected. This model gives good agreement with the data. In the second version, a significantly more complex version of their model, the FDF state space also includes velocity, and consequently, the direct effects of subgrid pressure fluctuations on the composition are included. Although this model produces a reasonable comparison to the data, the subgrid mixing rate that is driven explicitly by the stochastic velocity fluctuations is under-predicted. It is noted that despite their conceptual advantages, velocity-scalar FDF methods are relatively undeveloped in comparison to the more conventional scalar FDF methods, even in low-Mach flows.⁴⁴ This is a rather general issue³ that is not specific to MMC-LES, and it is therefore considered to be beyond the scope of the current work.

A. Compressible Eulerian LES equations

The filtered continuity equation is

$$\frac{\partial \bar{\rho}}{\partial t} + \frac{\partial}{\partial x_j} (\bar{\rho} \tilde{u}_j) = 0, \quad (1)$$

where t is the time, x is the spatial coordinate, $\bar{\rho}$ is the filtered density, and \tilde{u}_j is the Favre filtered j th velocity component. The filtered momentum equation is

$$\frac{\partial}{\partial t} (\bar{\rho} \tilde{u}_i) + \frac{\partial}{\partial x_j} (\bar{\rho} \tilde{u}_i \tilde{u}_j) + \delta_{ij} \frac{\partial \bar{p}}{\partial x_j} - \frac{\partial}{\partial x_j} (\tilde{\tau}_{ij} - \tau_{ij}^{\text{sgs}}) = 0, \quad (2)$$

where \bar{p} is the filtered pressure, δ_{ij} is a Kronecker delta function, and $\tilde{\tau}_{ij}$ is the molecular viscous stress tensor,

$$\tilde{\tau}_{ij} = \mu \left(\frac{\partial \tilde{u}_i}{\partial x_j} + \frac{\partial \tilde{u}_j}{\partial x_i} - \frac{1}{3} \delta_{ij} \frac{\partial \tilde{u}_k}{\partial x_k} \right). \quad (3)$$

Here, μ is the dynamic viscosity, which is calculated using the Sutherland formula. The Sub-Grid Scale (SGS) viscous stress tensor τ_{ij}^{sgs} is

$$\tau_{ij}^{\text{sgs}} = -\mu_t \left(\frac{\partial \tilde{u}_i}{\partial x_j} + \frac{\partial \tilde{u}_j}{\partial x_i} - \frac{1}{3} \delta_{ij} \frac{\partial \tilde{u}_k}{\partial x_k} \right) + \frac{1}{3} \delta_{ij} \bar{\rho} k_t, \quad (4)$$

where k_t is the SGS kinetic energy and μ_t is the SGS viscosity. The one-equation eddy-viscosity model is used, which solves the following transport equation for SGS kinetic energy:⁴⁵

$$\frac{\partial}{\partial t} (\bar{\rho} k_t) + \frac{\partial}{\partial x_j} (\bar{\rho} \tilde{u}_j k_t) - \frac{\partial}{\partial x_j} \left[(\mu + \mu_t) \frac{\partial k_t}{\partial x_j} \right] = -\tau_{ij}^{\text{sgs}} \frac{\partial \tilde{u}_i}{\partial x_j} - \frac{C_e \bar{\rho} k_t^{1.5}}{\Delta}, \quad (5)$$

where $C_e = 1.048$ is a model constant.⁴⁵ The SGS viscosity is estimated as $\mu_t = C_k \bar{\rho} \Delta_E \sqrt{k_t}$ with $C_k = 0.094$ being a model constant,⁴⁵ and Δ_E is the filter size estimated as the cube root of the LES cell volume.

Species and standardized enthalpy are FDF state space variables that are solved on the Lagrangian particles. For mass and energy consistency between the Eulerian and Lagrangian fields, additional

so-called *equivalent species* and *equivalent sensible enthalpy* transport equations are solved on the Eulerian grid.⁴² Essentially, sensible enthalpy and species mass fractions are coupled from the Lagrangian to the Eulerian fields, and the Eulerian density is then obtained through the equation of state (here, the ideal gas). The FDF species and enthalpy fields solved on the stochastic particles are considered to be the real fields, and the equivalent fields introduce a level of redundancy to ensure consistency. Full details and validation of the consistency of the Eulerian and Lagrangian fields are provided in Ref. 42, and only the essential details are repeated here.

The filtered equivalent sensible enthalpy equation reads

$$\begin{aligned} \frac{\partial}{\partial t} (\bar{\rho} \tilde{h}_s^E) + \frac{\partial}{\partial x_j} (\bar{\rho} \tilde{h}_s^E \tilde{u}_j) - \frac{D\bar{p}}{Dt} - \frac{\partial}{\partial x_j} \left(\bar{\rho} \mathcal{D}_{\text{eff}} \frac{\partial}{\partial x_j} \tilde{h}_s^E \right) \\ - \tilde{\sigma}_{ij} \frac{\partial \tilde{u}_i}{\partial x_j} = \frac{\bar{\rho} \left(\tilde{h}_s |f^E - \tilde{h}_s^E \right)}{\tau_{\text{rel}}}, \end{aligned} \quad (6)$$

where $D\bar{p}/Dt$ is the material derivative of pressure to account for the compressible pressure work, $\tilde{\sigma}_{ij} = \tilde{\tau}_{ij} - \bar{p} \delta_{ij}$, and $\mathcal{D}_{\text{eff}} = \mathcal{D}_m + \mathcal{D}_t$ is the sum of molecular and SGS thermal diffusivities. The molecular diffusivity is modeled as $\mathcal{D}_m = \mu / \bar{\rho} Sc$ with $Sc = 0.7$, and the SGS diffusivity is $\mathcal{D}_t = \mu_t / \bar{\rho} Sc_t$ with the turbulent Schmidt number $Sc_t = 0.4$.⁴⁶ The last term on the LHS of Eq. (6) denotes viscous heating. The filtered equivalent species equations are

$$\frac{\partial}{\partial t} (\bar{\rho} \tilde{Y}_m^E) + \frac{\partial}{\partial x_j} (\bar{\rho} \tilde{Y}_m^E \tilde{u}_j) - \frac{\partial}{\partial x_j} \left(\bar{\rho} \mathcal{D}_{\text{eff}} \frac{\partial}{\partial x_j} \tilde{Y}_m^E \right) = \frac{\bar{\rho} \left(\tilde{Y}_m |f^E - \tilde{Y}_m^E \right)}{\tau_{\text{rel}}}, \quad (7)$$

where \tilde{Y}_m^E is the filtered equivalent mass fraction of m th species. The source terms on the RHS of Eqs. (6) and (7) relax the Eulerian equivalent composition toward estimations of the conditional means in RMF space, $\tilde{h}_s |f^E$ and $\tilde{Y}_m |f^E$, which are obtained by integration over the stochastic particles with weighting by radial basis functions in both RMF and physical spaces. τ_{rel} is a relaxation time scale. The source terms here are not the same as those used in the quasi-laminar closures of the filtered source term, which neglect subgrid fluctuations. Here, the conditional means $\tilde{h}_s |f^E$ and $\tilde{Y}_m |f^E$ are estimated accurately from the stochastic particles and, therefore, explicitly include subgrid fluctuations. The turbulent fluctuations of equivalent sensible enthalpy and species mass fractions are driven by fluctuations in RMF. In Eqs. (6) and (7) and in the stochastic model below, unity Lewis number is used for all the species, whereas the molecular and turbulent Prandtl numbers are 0.7 and 0.4, respectively. A review of the literature suggests that these settings are conventional for this flame case where subgrid turbulent diffusion is likely to be larger than molecular diffusion,^{9,47–52} and recently, Zheng and Yan⁵³ demonstrated a low sensitivity over a range of reasonable turbulent Prandtl and Schmidt numbers.

The transport equation for filtered RMF (\tilde{f}), which is also used for localizing stochastic particle mixing described below, has the same form as Eq. (7) but with zero source term since it is a conserved normalized scalar with $\tilde{f} = 1$ in the fuel stream and $\tilde{f} = 0$ in the oxidizer stream,

$$\frac{\partial}{\partial t} (\bar{\rho} \tilde{f}) + \frac{\partial}{\partial x_j} (\bar{\rho} \tilde{f} \tilde{u}_j) - \frac{\partial}{\partial x_j} \left(\bar{\rho} \mathcal{D}_{\text{eff}} \frac{\partial}{\partial x_j} \tilde{f} \right) = 0. \quad (8)$$

B. Compressible stochastic differential equations on Lagrangian particles

The SDEs for the evolution of the joint FDF of species mass fractions and standardized enthalpy are³⁴

$$dx_i^q = \left[\tilde{u}_i + \frac{1}{\bar{\rho}} \frac{\partial}{\partial x_i} (\bar{\rho} \mathcal{D}_{eff}) \right]^q dt + \delta_{ij} (\sqrt{2\mathcal{D}_{eff}})^q d\omega_i, \quad (9)$$

$$dY_m^q = (W_m^q + S_m^q) dt, \quad (10)$$

$$dh^q = \left[W_h^q + S_h^q + \left(\frac{1}{\bar{\rho}} \frac{D\bar{p}}{Dt} \right)^q + \left(\frac{1}{\bar{\rho}} \tilde{\sigma}_{ij} \frac{\partial \tilde{u}_i}{\partial x_j} \right)^q \right] dt, \quad (11)$$

$$\langle S^{p,q}[\tilde{f}, \mathbf{x}] \rangle = 0. \quad (12)$$

Here, q is a particle index associated with a stochastic realization of the turbulent field and \mathbf{x} is a position vector. Equation (9) is for transport of particles in physical space where $d\omega_i$ is the increment of an independent Wiener process. Equations (10) and (11) govern the transport of particle mass fractions, Y_m^q , and standardized enthalpy, $h^q = (h_f^0 + \int_{T_0}^T C_p dT)^q$, where W_m^q is the closed non-linear chemical source term and W_h^q is the radiative heat loss (set to zero here). The pressure work and viscous heating are incorporated in Eq. (11) to account for the compressibility effects in supersonic flows. S_m^q and S_h^q are the mixing terms to account for the dissipation of conditional subfilter fluctuations of mass fractions and standardized enthalpy, respectively. Equation (12) represents the mixing constraint to conserve conditional means imposed by the MMC model through enforcing mixing localness in a combined space comprised of RMF, \tilde{f} , and position, \mathbf{x} . This conservation of conditional means (which is also the central concept in the CMC model¹⁷) permits a sparse particle resolution in \mathbf{x} -space, provided that particles mix locally in \tilde{f} -space. The particular form of the mixing operation used here adopts a variant of the Curls mixing model.⁵⁴ Particles are mixed in pairs (particles p and q) where the mean distance between the mixing pairs in (\mathbf{x}, \tilde{f}) -space is controlled by global model parameters r_m , the characteristic distance in \mathbf{x} -space, and f_m , the characteristic distance in \tilde{f} -space. Here, $f_m = 0.01$,⁵⁵ and r_m is obtained by the fractal model developed in Ref. 35. The pairwise mixing is linear and has a mixing time scale, τ_L , and here, the a-ISO time scale model is used.⁴¹

C. Numerical implementation

The governing equations are implemented in the validated, hybrid Lagrangian–Eulerian solver called *mmcFoam*⁴² that is compatible with OpenFOAM. For supersonic and highly compressible flows, the Eulerian equations in OpenFOAM are solved using the density-based central scheme called *rhoCentralFoam*.⁵⁶ It employs the KNP method of Kurganov, Noelle, and Petrova⁵⁷ with van Leer limiting and has been applied to various non-reacting benchmark tests including the one-dimensional Sod's problem, two-dimensional forward-facing step, and supersonic jet flows by Green-shields *et al.*⁵⁶ who demonstrated the ability to capture sharp discontinuities due to shocks without inducing oscillations. The central scheme has also been validated for turbulent, high-speed reacting

flows (without the MMC combustion model) in our recent work on an auto-igniting cavity stabilized ethylene flame⁵⁸ and a coflow hydrogen jet flame⁵⁹ and also by others, e.g., the work of Wu *et al.*,⁹ Ye *et al.*,^{60,61} and Wu *et al.*⁶²

The finite volume form of the Eulerian LES equations for momentum and enthalpy [Eqs. (2) and (6)] is integrated with a low-cost, operator-splitting method.⁵⁶ In the first step, explicit predictor equations are solved for the convection of conserved momentum and equivalent sensible enthalpy,

$$\frac{\partial}{\partial t} (\tilde{M}_j) + \nabla \cdot (\tilde{U} \tilde{M}_j + \tilde{p} \delta_{ij}) = 0, \quad (13)$$

$$\frac{\partial}{\partial t} (\tilde{H}_s^E) + \nabla \cdot (\tilde{U} \tilde{H}_s^E) - \tilde{\sigma}_{ij} \nabla \cdot \tilde{U} = 0, \quad (14)$$

where $\tilde{M}_j = \bar{\rho} \tilde{u}_j$, $\tilde{U} = (\tilde{u}_i, \tilde{u}_j, \tilde{u}_k)$ is the filtered velocity vector, $\nabla \cdot \mathbf{F}$ is the divergence of vector $\mathbf{F} = (F_x, F_y, F_z)$, and $\tilde{H}_s^E = \bar{\rho} \tilde{h}_s^E - \tilde{p}$. The second-order semi-discrete, non-staggered, central-upwind scheme (i.e., KNP method⁵⁷) is used for the spatial discretization in Eqs. (13) and (14). In the second step, corrector equations are solved for the diffusion of the primitive velocity and equivalent sensible enthalpy variables

$$\frac{\partial}{\partial t} (\bar{\rho} \tilde{u}_j)^i - \frac{\partial}{\partial t} (\bar{\rho} \tilde{u}_j)^e - \frac{\partial}{\partial x_j} (\tilde{\tau}_{ij} - \tau_{ij}^{sgs}) = 0, \quad (15)$$

$$\frac{\partial}{\partial t} (\bar{\rho} \tilde{h}_s^E)^i - \frac{\partial}{\partial t} (\bar{\rho} \tilde{h}_s^E)^e - \frac{\partial}{\partial x_j} \left(\bar{\rho} \mathcal{D}_{eff} \frac{\partial}{\partial x_j} \tilde{h}_s^E \right) = \frac{\bar{\rho} (\tilde{h}_s \tilde{f}^E - \tilde{h}_s^E)}{\tau_{rel}}, \quad (16)$$

where $(\bar{\rho} \tilde{u}_j)^i$ and $(\bar{\rho} \tilde{h}_s^E)^i$ are discretized implicitly, while $(\bar{\rho} \tilde{u}_j)^e$ and $(\bar{\rho} \tilde{h}_s^E)^e$ are discretized explicitly using the known values from Eqs. (13) and (14), respectively. The convective transport terms for the bounded scalar quantities, namely, SGS kinetic energy transport equation [Eq. (5)], equivalent species mass fractions [Eq. (7)], and RMF [Eq. (8)], are discretized with a Total Variation Diminishing (TVD) scheme. To minimize non-orthogonality errors, the diffusive terms in Eqs. (5), (7), (8), (13), and (16) are split into orthogonal and non-orthogonal parts.⁶³ For the former, a second-order Gauss scheme with linear interpolation is used, and for the latter surface, interpolation of variable normal gradients is applied. All Eulerian transport equations are temporally discretized with a second-order implicit Crank–Nicolson scheme.

The stochastic Lagrangian transport equations (9)–(12) are integrated as three fractional steps. Spatial transport in Eq. (9) uses the first-order Euler–Maruyama scheme.⁶⁴ Chemical source terms are integrated in time using a stiff ODE solver called *seulex*.⁶⁵ The particle pairs for the mixing are selected dynamically using a k -dimensional tree algorithm.⁶⁶ Full details are provided in Ref. 42.

Instantaneous two-way coupling is implemented between the Eulerian LES fields and Lagrangian particles. To solve the SDEs, the filtered velocity, pressure and its material derivative, and RMF and SGS diffusivity from the Eulerian LES are tri-linearly interpolated at particle locations. As mentioned earlier and in line with other FDF work,³³ the SGS contributions of the filtered pressure are not considered in this interpolation and the same applies to the viscous heating terms. Meanwhile, density is passed from the Lagrangian

field to the LES. Due to the stochastic nature of Lagrangian density and the sparse distribution of particles, this density transfer is non-trivial and necessitates the solution of the filtered equivalent sensible enthalpy and composition fields through Eqs. (6) and (7).

III. CASE CONFIGURATION

A. Experimental configuration

The target experimental configuration is a hydrogen-fuelled, strut-based model supersonic combustor.⁴³ A two-dimensional slice of the three-dimensional domain is shown in Fig. 1. The combustor height (y -direction) at the entrance is 50 mm, and the total length (x -direction) is 340 mm. The width (z -direction, not shown) is 45 mm. The wedge-shaped strut is 6 mm high by 32 mm long and is placed at the combustor centerline, a distance of 77 mm downstream of the entrance. Around the downstream surface of the strut, at $x = 109$ mm, there are 15 circular hydrogen (H_2) injectors. The upper combustor wall has a divergence angle of 3° starting at $x = 100$ mm to compensate for the boundary layer expansion.⁴³ The experimental data of mean and Root-Mean-Square (rms) fluctuations of axial velocity at different streamwise locations, bottom wall pressure, as well as schlieren images are available for both non-reacting and reacting cases. The time-averaged temperature at different stream-wise locations and velocity along the centerline are also available for the reacting case.

The experimental inlet boundary conditions for both non-reacting and reacting cases are given in Table I, where p is the pressure, T^* is the stagnation temperature, Ma is the Mach number, k_t is the turbulent kinetic energy, and Y_m is the mass fraction of species m . Specifically, air enters the combustor at $Ma = 2.0$ with a stagnation temperature of 600 K and a static pressure of 0.1 MPa. Hydrogen is injected sonically at a stagnation temperature of 300 K and a static pressure of 0.1 MPa. The global equivalence ratio is 0.034. Note that the inlet pressure, temperature, and velocity are time-averaged values. The inflow Reynolds numbers estimated based on the inlet conditions for air and hydrogen are 1.78×10^6 and 6.67×10^3 , respectively.

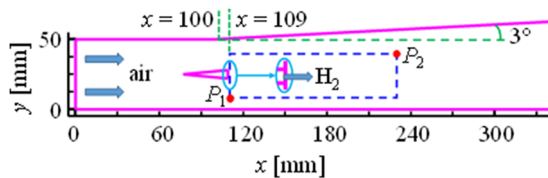


FIG. 1. Two-dimensional schematic of the model supersonic combustor.⁴³ Domain P_1 – P_2 behind the strut is for visualization in Figs. 11, 13(a), and 13(b).

TABLE I. Inlet boundary conditions.⁴³

Inlet	p (MPa)	T^* (K)	Ma	k_t (m^2/s^2)	Y_{O_2}	Y_{H_2O}	Y_{N_2}	Y_{H_2}
Air	0.1	600	2.0	10	0.232	0.032	0.736	0.0
H_2	0.1	300	1.0	2400	0.0	0.0	0.0	1.0

B. Eulerian computational configuration

The Eulerian computational domain is discretized using 4 866 900 hexahedrons. The minimum grid size is 0.11 mm, 0.07 mm, and 0.07 mm in x , y , and z directions, respectively. The time step used is 10^{-9} s, corresponding to a maximum Courant number of about 0.1. This grid resolution is chosen based on our previous LES of the same combustor with a Partially Stirred Reactor (PaSR) combustion model^{49,50} and is also comparable with those of Wang *et al.*⁴⁸ and Wu *et al.*⁵¹ The grid is clustered around the injector in the combustor and the regions after the strut where strong mixture gradients exist. *A posteriori* analysis of one of the present reacting MMC-LES (case 3, which is detailed later in Table II) indicates that the spatially averaged y^+ value at the strut wall is less than 1.0. The resolution near the external combustor walls is similar although slip boundary conditions are applied there as those walls have negligible effects on the mixing and combustion processes in the central region of the combustor as found in our recent work.⁵⁹ Hence, the Shock/Boundary Layer Interactions (SBLIs) on the combustor walls are not accounted for in this work as previous work has indicated that they have negligible effects on the central combustion regions.⁶⁷ A further measure of the grid resolution is obtained from the ratio of the SGS viscosity to the molecular viscosity,^{5,68}

$$\mu_E = \frac{\mu_t}{\mu}. \quad (17)$$

Figure 2 shows an instantaneous scatter plot of μ_E vs the filtered heat release rate colored by the temperature scale at the combustor central-plane for the same case 3. For most of the regions with a significant heat release rate (i.e., $\tilde{q} \geq 1 \times 10^9$ W/m³, which is greater than 5% of the highest value), the corresponding values of μ_E are less than 3 (bounded by the pink dashed box in Fig. 2). These data points satisfy the well-resolved LES criterion of Bouharaoua *et al.*⁵ Only a small number of data points have $\mu_E \geq 3$, and these correspond to the locations of low temperature and low heat release rate (typically less than 1×10^9 W/m³) outside the main combustion area of interest.

Supersonic Dirichlet boundaries are specified at both the air and hydrogen inlets. Previous work on this combustor^{9,49–51} shows that interactions between the neighboring fuel jets is small, and the injection may be treated as being quasi-two-dimensional. Therefore, a simplified single injector configuration (2.4 mm wide in the z -direction) is used here. To retain the global equivalence ratio, the diameter of the injector is adjusted to be about 0.9 mm. This simplification does not significantly change the injector surface to volume ratio and, as confirmed in Sec. IV A, is sufficient to reproduce the main flow structures including shocks, expansion fans, and shear layers between the central subsonic zone and supersonic air inflow.

TABLE II. Information for test cases.

Case no.	N_p	R_{LE}	Δ_L (mm)	Note
1	973 380	1L/5E	0.135	Non-reacting with Dp/Dt
2	486 690	1L/10E	0.173	Reacting with Dp/Dt
3	973 380	1L/5E	0.135	Reacting with Dp/Dt
3a	973 380	1L/5E	0.135	Reacting without Dp/Dt
4	1 622 300	1L/3E	0.115	Reacting with Dp/Dt

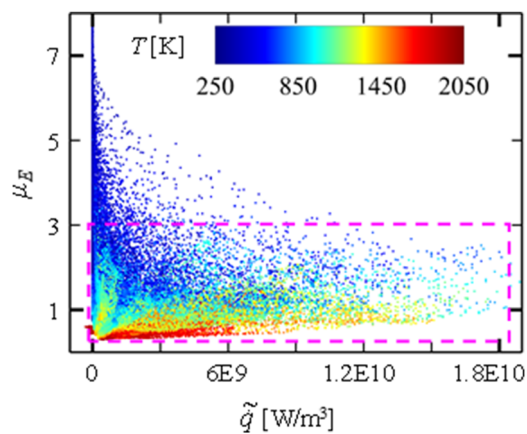


FIG. 2. Instantaneous scatter plot of μ_E vs \tilde{q} colored by the temperature scale for case 3.

Based on the experimental values of k_t , the inlet velocity has turbulent fluctuations of 3.3% and 0.35% of the mean values at the air and hydrogen inlets, respectively. Since the outflow is supersonic, zero gradient conditions are applied at the outlet boundary for all variables.

C. Lagrangian computational configuration

As this is the first application of MMC-LES to supersonic flows, a number of computational configurations are tested, as indicated in Table II to analyze the sensitivity to the sparse stochastic particle resolution. Additionally, we examine the importance of the compressible pressure work term in Eq. (11), which has been neglected in previous MMC-LES. Note that the viscous heating term for the present combustor configuration is a factor of at least 1000 times smaller than the pressure work term and may be neglected. The non-reacting case 1 is compared to the experimental data for mean and rms of axial velocity at different streamwise locations and the central-plane schlieren image in order to validate the solver's capability to capture discontinuities and fluid mixing. The reacting cases are tested for three different particle resolutions. Here, N_p is the total number of particles in the domain, and results are obtained over a fourfold variation. R_{LE} is the ratio of Lagrangian particles to Eulerian LES cells (all have fewer particles than cells and are therefore considered sparse), and Δ_L is the nominal spatial distance between the particles. Case 2 is the sparsest case, while case 4 is the densest case. A particle number control algorithm is employed by cloning or killing particles if the number falls below or above the lower and upper limits, respectively.⁴²

Stochastic particle chemical kinetics uses an improved version of Marinov's detailed hydrogen oxidation chemistry containing nine species (H_2 , O_2 , N_2 , H_2O , HO_2 , H_2O_2 , H , O , and OH) and 27 elementary reactions (including reverse reactions).⁶⁹ It has been extensively validated by Marinov *et al.* and is found to reproduce experimental laminar flame speed, flame compositions, and shock tube ignition delay times accurately.⁶⁹ In the Appendix, further comparisons are made for ignition delay time and laminar flame speed with the experimental data,^{70,71} and good accuracy of this mechanism

can be observed for operating conditions relevant to supersonic combustion.

IV. RESULTS AND DISCUSSION

To ensure convergence following an initial purge of the field (3.5 ms from the initial injection), the stationary statistical results presented in this section were compiled over an additional flow time of 4.5 ms corresponding to about ten characteristic domain flow-through times (estimated based on the combustor length and air inlet velocity). Simulations were performed on 60 bi-processors with 2.60 GHz cores on the ASPIRE 1 Cluster at the National Supercomputing Centre in Singapore. The computational time for case 3 is about 14 300 CPU-h per flow-through time, of which ~79.3% is associated with the Eulerian scheme (including the solution of the equivalent species and sensible enthalpy equations for the density coupling between Eulerian and Lagrangian fields) and 20.7% is associated with the Lagrangian scheme on which the chemistry is integrated. As a comparison, the Quasi-Laminar Chemistry (QLC) LES of this same combustor (simulated with an identical chemical mechanism, mesh, and turbulence model) in our recent work⁵⁹ has a similar overall computational cost (16 080 CPU-h per flow-through time) of which ~44.4% is associated with integration of the chemical kinetics. These breakdowns and the similarity of the total cost, despite far fewer Lagrangian particles than LES cells, illustrate the relatively low computational load for integration of the simple hydrogen scheme used in the present work. The cost savings of sparse MMC-LES increase significantly with the complexity of the fuel and the required kinetics scheme.

A. Non-reacting case

Figure 3 shows the cross-stream profiles of mean axial velocity (u_{x-avg}) and rms fluctuations (u_{x-rms}) at various streamwise locations for case 1. For comparison, we also include the LES results of Fureby *et al.*⁷² and Génin and Menon.⁷³ In Ref. 72, a full width combustor (with 15 fuel injectors), 22.5×10^6 cells, and a mixed model (the scale-similarity model mixed with a diffusive subgrid viscosity model) are used. In Ref. 73, two fuel injectors, 2.5×10^6 cells, and the dynamic one-equation eddy-viscosity SGS kinetic energy model are used. The mean velocity is well predicted at all locations in the present work and has comparable accuracy to the results of Génin and Menon and is slightly better than the results of Fureby *et al.*, which exhibit somewhat larger deviations in the central mixing regions at $x = 120$ mm and 167 mm. The rms predictions in Fig. 3 are also quite well predicted at the two locations where the experimental data are available. The slight under-prediction of u_{x-rms} in the present simulations around the combustor centerline is similar to the findings of Génin and Menon.

Figure 4 shows the contours of mean and instantaneous magnitude of density gradient ($|\nabla\rho|$) along with the experimental schlieren image for case 1.⁴³ Overall, the predicted flow structures including shocks, expansion fans, and shear layers between the central mixing zone and the supersonic air stream are qualitatively similar to those observed experimentally and bear close resemblance to those reported in Refs. 72 and 73. Specifically, the axial intersection point of the two reflected shocks at the central shear layers at $x \approx 142$ mm (line 1), the incident points of the expansion fan and reflected shock

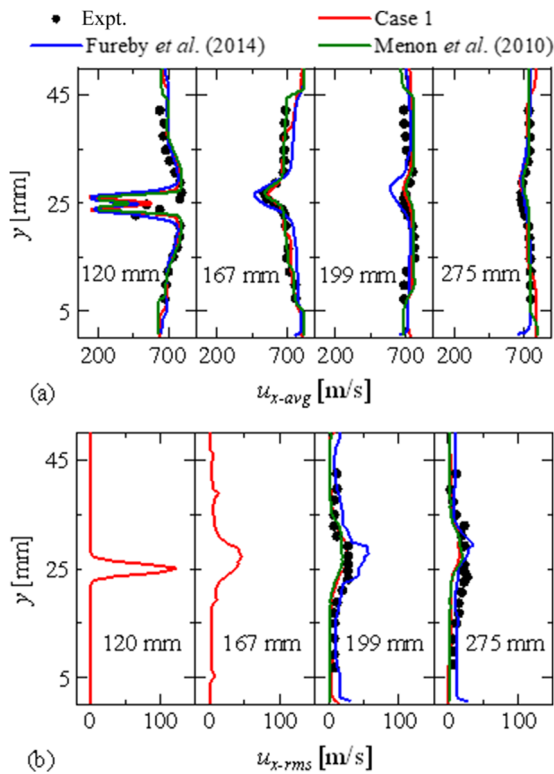


FIG. 3. Profiles of axial velocity statistics at different streamwise locations for the non-reacting case 1: (a) mean and (b) rms. The results are compared with the work of Génin and Menon,⁷³ the work of Fureby *et al.*,⁷² and experimental data.⁴³

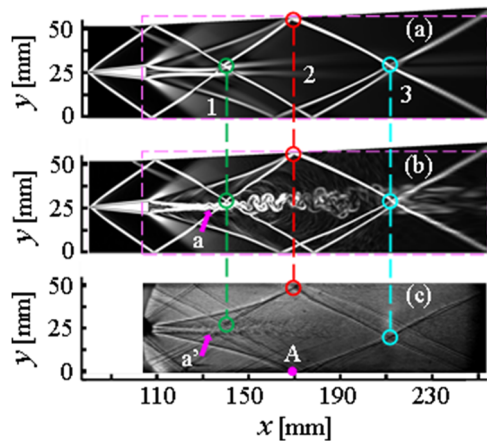


FIG. 4. Contours of (a) mean and (b) instantaneous density gradient magnitude, and (c) experimental schlieren image⁴³ for the non-reacting case 1. Lines 1, 2, and 3 indicate the intersection point of the two wall-reflected shocks, the incident point of the expansion wave on the upper combustor wall, and the intersection point of the two wall-reflected expansion fans, respectively. The arrows a and a' indicate the destabilization of the eddies along the mixing layer after the strut, and the dashed boxes indicate the same domain to the experimental schlieren.

at the upper combustor wall at $x \approx 170$ mm (line 2), and the intersection point of the two reflected expansion fans downstream at $x \approx 212$ mm (line 3) are all well predicted by our LES. Comparison of the instantaneous images in Figs. 4(b) and 4(c) also indicates that the LES quite accurately predicts the point of destabilization of the fuel/air interface and the start of lateral growth of eddies in the mixing layer (see the arrows a and a'). Clearly, there is good similarity between the simulations and the experiments in the central region of the flow where mixing occurs. However, Fig. 4 also reveals that there is a more complicated shock and expansion fan structure along the bottom wall than the top wall. On the top wall, the reflected shocks coincide quite neatly at the location indicated by line 2. On the bottom wall, near point A, the reflected shocks do not intersect on the wall, and there are likely to be significant interactions with the boundary layer in the experiment. Although the predictions and experiments show qualitative similarity along the bottom wall, there are slight differences between them although these are hard to judge as the experimental image lacks a strong contrast in color shades. As mentioned already, the LES does not capture SBLIs, and this may contribute to differences in the shock structure.

To explore the capability of the Lagrangian scheme to capture discontinuities and the contribution of pressure work to the overall standardized enthalpy of the gas, Fig. 5 shows the instantaneous standardized enthalpy, h^q , and the pressure work fraction, $\eta^q = \left[\frac{1}{\rho} \frac{Dp}{Dt} \right]^q / \left(\frac{dh^q}{dt} \right)$, on Lagrangian stochastic particles for case 1. Here, h^q has been clipped to the range of 0 MJ/kg–0.1 MJ/kg to highlight the effect of the Dp/Dt term near the shocks and expansion fans. Note that the central jet region has much higher enthalpy due to the injection of the fuel. It is seen that h^q generally increases in post-shock regions (due to the compression work input from the surrounding gas) and decreases in the expansion fans (due to the work done on the surroundings). In Fig. 5(b), the maximum

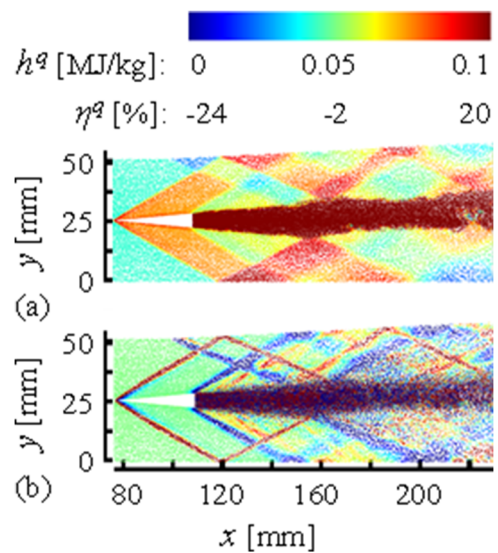


FIG. 5. Instantaneous distributions of particles colored by (a) h^q and (b) η^q in the non-reacting case 1.

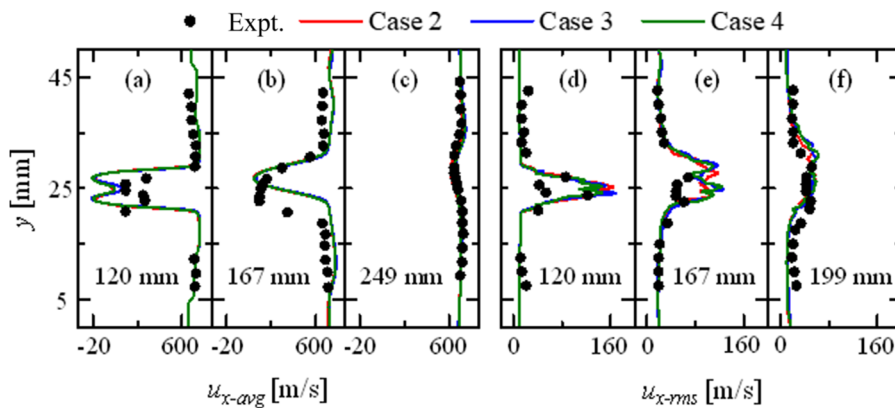


FIG. 6. Profiles of axial velocity statistics at different streamwise locations for the reacting cases 2–4. [(a)–(c)] mean and [(d)–(f)] rms. Experimental data from Ref. 43.

η^q of 19.2% occurs at shock fronts, whereas the minimum value of -23.8% occurs at the expansion fans. Beyond these discontinuities (shocks and expansion fans), the pressure work effect is not significant and corresponds to only a few tenths of a percent of the total standardized enthalpy.

B. Mean results and sensitivity to stochastic particle number in reacting cases

Figure 6 shows the cross-stream profiles of mean and rms of axial velocity at different streamwise locations in the reacting flows. The results are shown for MMC-LES cases 2, 3, and 4 with a fourfold variation in stochastic particle number, N_p . The negligible differences between these predictions indicate that there is a low sensitivity of velocity to N_p and hence a low sensitivity to the mean particle mixing distance, R_{LE} . In comparison to the experimental data, the mean velocity is well predicted at most locations. There is slight overshoot at $x = 120$ mm near where the recirculation behind the strut breaks down, and this is consistent with earlier LES using the partially stirred reactor model,^{49–51,72} the flamelet model,⁴⁸ and the Eulerian stochastic fields PDF method.⁵² For the three axial locations shown, the rms velocities are captured reasonably well, especially at $x = 120$ mm and 199 mm. At $x = 167$ mm, relatively large deviations are seen in the central combustion zone. This may result from the strong unsteadiness around the end of the recirculation zone ($x \approx 150$ mm based on our LES). A similar over-prediction of u_{x-rms} around the combustor centerline at $x = 167$ mm is also seen in other studies.⁷²

Figure 7 shows the profiles of mean temperature (T_{avg}) at different streamwise locations for cases 2–4. There is again a very low sensitivity to the particle number. In the central combustion zone at $x = 120$ mm and 167 mm, T_{avg} is slightly under-predicted, whereas at $x = 275$ mm, it is predicted very well. Figure 8 shows the centerline (at $y = 25$ mm) profiles of mean axial velocity and pressure along the bottom wall of the combustor (at $y = 0$ mm). Figures 7 and 8 demonstrate good predictions for u_{x-avg} and p_{avg} , respectively, and both demonstrate a very low sensitivity to the number of stochastic particles. The under-prediction of u_{x-avg} in the strut wake zone in Fig. 8(a) is also found in other LES work^{49–51,72,73} and may be caused by the turbulence of the H_2 jet. Note that there are no direct experimental data for the inlet velocity fluctuations, and hence, the

accurate reproduction of the real inlet turbulence is difficult in our LES. The pressure predictions follow the correct trend with the axial position, but there is under-prediction further downstream. This may be associated with a late pressure rise due to the unresolved SBLI and subsequent axial location inaccuracies in the reflected shocks along the bottom wall. Furthermore, this is a common problem in other relevant studies,^{47,51,52,72,73} regardless of the SGS combustion models used.

The above statistics of MMC-LES in Figs. 6–8 are generally better predicted compared with those of the QLC-LES in the previous work for this same combustor,⁵⁹ especially in the downstream locations. Note that in the upstream (e.g., before $x = 199$ mm), the QLC-LES is highly resolved as it has been demonstrated in Fig. 11 of Ref. 59, and therefore, the QLC-LES also gives good predictions there. After $x = 199$ mm, the MMC-LES gives better predictions even with only one particle for every ten LES cells (case 2).

Figure 9 shows the scatter plots of temperature and H_2O and OH mass fractions in mixture fraction space for cases 2–4 colored by the streamwise location. The data points are instantaneous values on the stochastic particles, and the figures are obtained by collecting the ensemble over time. Localized extinctions are most pronounced

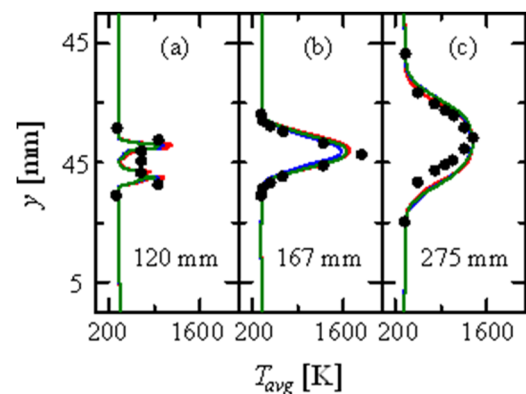


FIG. 7. Profiles of the mean temperature at different streamwise locations for the reacting cases 2–4. Experimental data from Ref. 43. The legend is the same as in Fig. 6.

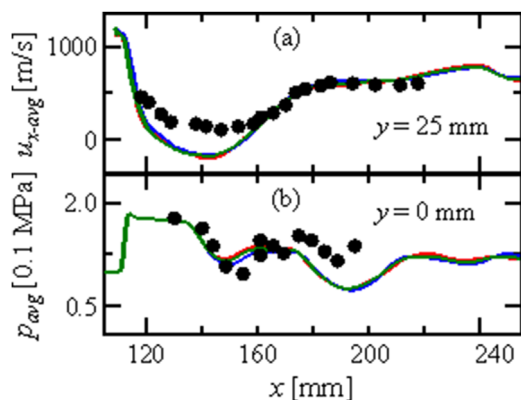


FIG. 8. Streamwise profiles of mean (a) axial velocity and (b) bottom wall pressure for the reacting cases 2–4. Experimental data from Ref. 43. The legend is the same as in Fig. 6.

upstream where TCI are significant, and the flame structure returns toward equilibrium downstream. Generally, the results of the three cases with various numbers of particles are quite close at three locations, indicating a low sensitivity to the sparse particle number. Some minor differences are observable in the OH mass fraction. For instance, for the OH mass fraction at $x = 199$ mm in case 3, there are slightly fewer particles present that have reactive and intermediate states, which may lead to slight underestimations of the instantaneous localized extinction and re-ignition. However, the location $x = 199$ mm is far from the strut base ($x = 109$ mm) as well as the flame base ($x \approx 138$ mm) and hence has a limited effect on the upstream flame dynamics. Further exploration of the flame structure and sensitivity to the particle number is given in Fig. 10, which shows the mean and rms of temperature and H_2O and OH mass fractions conditioned on the mixture fraction, z . The substantial departure from equilibrium is evident at the most upstream location through the lower peak mean conditional temperature and OH mass fraction. The conditional means have virtually no sensitivity to the particle

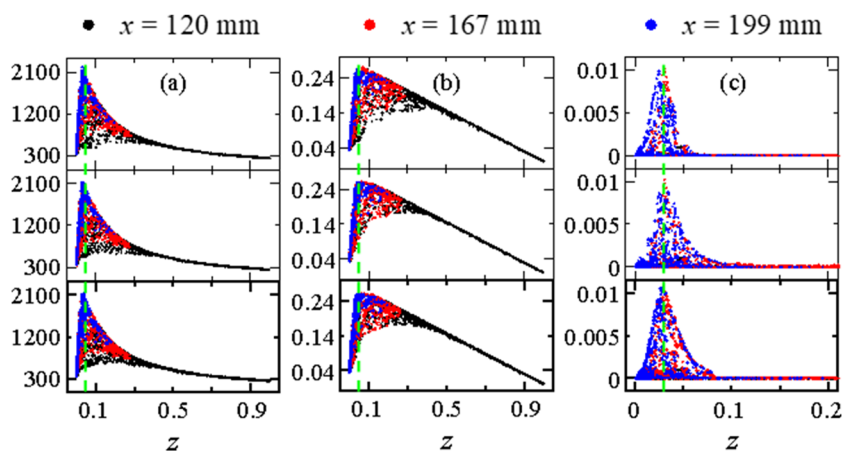


FIG. 9. Scatter plots of (a) temperature, (b) H_2O mass fraction, and (c) OH mass fraction vs mixture fraction at different axial locations for the reacting cases 2 (top), 3 (middle), and 4 (bottom). The green dashed line indicates the stoichiometric mixture fraction.

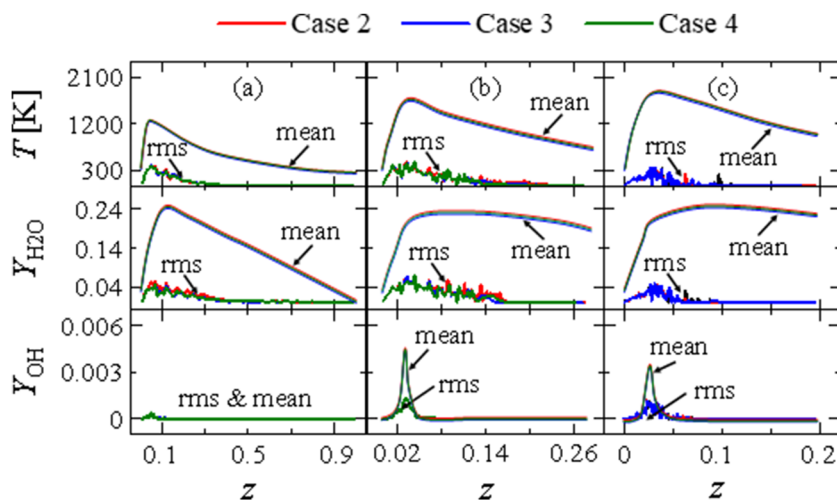


FIG. 10. Conditional mean and rms of temperature (first row), H_2O (second row), and OH (third row) mass fractions at axial locations of (a) $x = 120$ mm (first column), (b) $x = 167$ mm (second column), and (c) $x = 199$ mm (third column) for cases 2–4.

number. The conditional rms has stronger stochastic errors when fewer particles are used, but this is improved if the temporal averaging period is increased, and most importantly, due to the MMC model preserving conditional means in mixture fraction space, there is no bias error evident in the results for the cases using fewer particles. The predictions of other major and minor reactive scalars (e.g., H_2 and O_2 mass fractions, not shown) exhibit a similar low sensitivity to the particle number.

Overall, all the results in Figs. 6–10 demonstrate a low sensitivity to the number of particles, which is expected due to the enforcement of mixing localness in reference mixture fraction space, and that good results can be obtained with as few as one stochastic particle for every ten LES cells. This is in agreement with MMC-LES of low-Mach combustion cases.

C. Flame dynamics

In this section, case 3 is selected for further analysis of the unsteady flame dynamics. Figure 11 shows the instantaneous contours of temperature, heat release rate, and OH mass fraction for the sub-domain P_1 – P_2 (see Fig. 1). The mean position of the flame base is indicated by line A (at $x \approx 138$ mm) in Fig. 11(a), which is defined as the first axial occurrence where $T_{avg} = 1450$ K. Based on our tests, choosing other reasonable threshold values of T_{avg} , or indeed other quantities (e.g., reaction rate of H_2), does not cause an obvious change of the identified flame base locations. The flame base is stabilized in a central recirculation zone that extends from $x = 109$ mm to $x \approx 159$ mm on the downstream side of the fuel

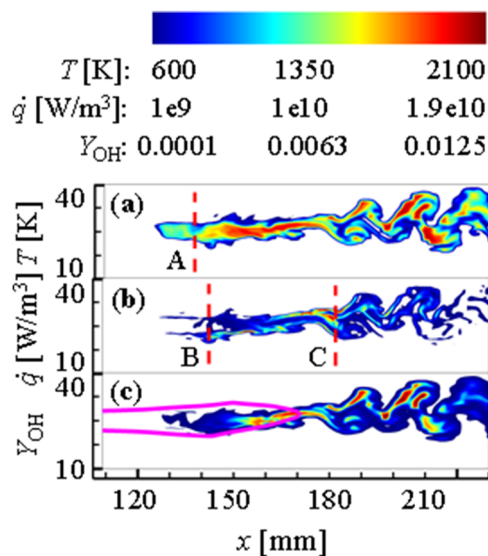


FIG. 11. Contours of (a) temperature, (b) heat release rate, and (c) OH mass fraction from the reacting case 3. The results are for the equivalent species and equivalent sensible equations and are approximations of the instantaneous filtered fields. Line A indicates the mean position of the flame base, and lines B and C indicate the boundaries of the reaction induction zone, transitional zone, and turbulent combustion zone. The pink line in Fig. 11(c) is the stoichiometric iso-line, i.e., $z_{st} = 0.0283$. The starting point of the x-axis lies at the rear edge of the strut (i.e., $x = 109$ mm).

strut. For axial locations upstream of line B ($x \approx 142$ mm), the rather straight property contours indicate that there is very little spanwise turbulent mixing in the shear layer between the fuel jet and the air stream. From line B to line C ($x \approx 182$ mm), turbulent mixing in the shear layer increases somewhat and combustion can be observed with rapid streamwise increases in T , \dot{q} , and Y_{OH} . Downstream of location C, large scale vortices appear along the shear layer, and there are considerable spanwise variations in the flame. The three zones A–B, B–C, and downstream of C, which may be broadly classified as reaction induction, transitional, and turbulent combustion zones, are found to be in good agreement with those reported in Refs. 50 and 72.

Figure 12 shows the contours of mean and instantaneous magnitude of density gradient, as well as the experimental schlieren image for the reacting case.⁴³ Once again, flow structures including shocks, expansion fans, and shear layers between the central recirculation zone and supersonic air stream are clearly seen and bear close resemblance to those reported elsewhere.^{50,51,72,73} Specifically, the incident points of the two reflected shocks at the central shear layers at $x \approx 140$ mm and 150 mm (indicated by the dotted lines 1 and 2 with circles) are well predicted by LES in comparison to the experimental schlieren image. The destabilization of the eddies along the shear layer (see the dashed line 3) is also well captured in our LES. The accurate reproduction of the shock incidence location around the flame is important in this case, since it may enhance the local chemical reactions due to elevated pressure and therefore improve the flame stability.⁵⁰ This is further analyzed in Figs. 13 and 14.

Figures 13(a) and 13(b) show the instantaneous h^q on Lagrangian particles for cases 3a and 3, respectively, and the differences between them allow us to examine the magnitude and effects

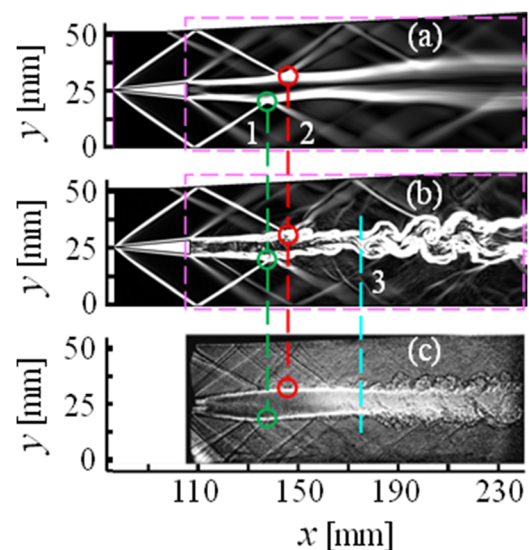


FIG. 12. Contours of (a) mean and (b) instantaneous magnitude of density gradient, and (c) experimental schlieren image⁴³ for the reacting case 3. Lines 1 and 2 indicate the incident points of the lower and upper wall reflected shocks at the central shear layer, respectively, whereas line 3 indicates the destabilization of the shear layer. The dashed boxes indicate the same domain to the experimental schlieren.

of pressure work. Difference can be found, especially in the strut wake zone, where h^q is generally higher when the Dp/Dt pressure work term is included. This is particularly noticeable in the reaction induction zone ($x < 142$ mm). Consequently, this may affect the transient flame dynamics, specifically the fluctuations of the flame base locations (shown later in Fig. 14). Figure 13(c) shows h^q in a narrower magnitude range for case 3 to highlight the effect of the Dp/Dt term near the shocks and expansion fans. The overall distribution of h^q is similar to the counterpart of the non-reacting case 1 shown in Fig. 5(a), especially in the coflow regions, while the central region downstream of the strut in Fig. 13(c) is broadened in the reacting case. Figure 13(d) shows the pressure work fraction η^q for case 3. The maximum value of η^q is about 18.6% at the shock fronts, slightly lower than the corresponding value (19.2%) for the non-reacting case. This may be due to the fact that the overall pressure

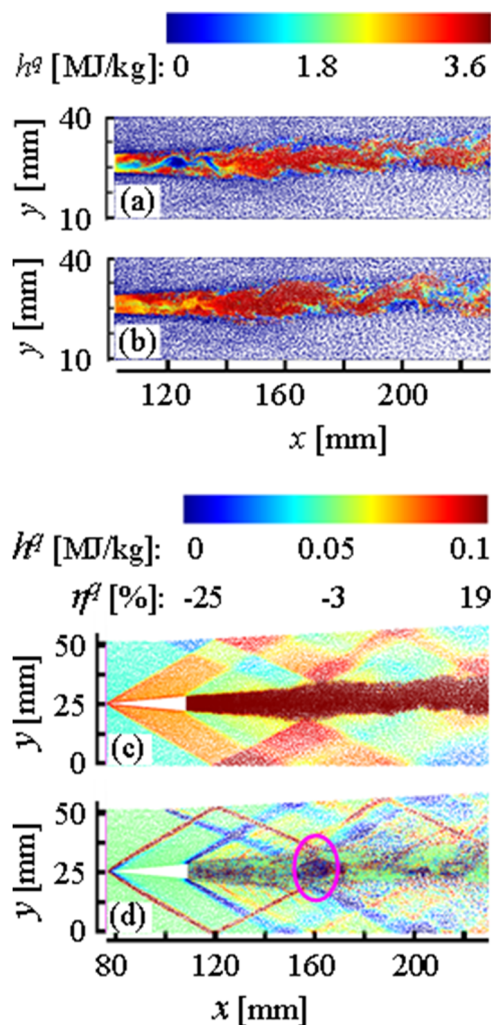


FIG. 13. Instantaneous distributions of particles colored by (a) h^q in case 3a without Dp/Dt , (b) h^q in case 3 with Dp/Dt , (c) h^q (range clipped: 0 MJ/kg–0.1 MJ/kg) in case 3 with Dp/Dt , and (d) η^q in Case 3 with Dp/Dt .

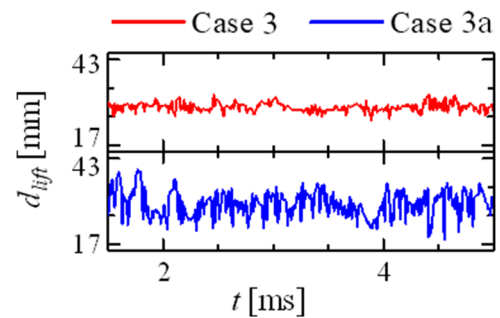


FIG. 14. Time evolutions of flame lift-off distance for cases 3 and 3a.

in the combustor section after the strut is slightly higher when combustion is occurring, which decreases the pressure ratio and hence the pressure work across the shock front. The minimum value of η^q is about -24.5% in case 3 at the expansion fan, also slightly lower than the value of -23.8% observed for the non-reacting case. The reason may be similar; as the expansion fan has a smaller margin to expand with higher back pressure for the present reacting case, and consequently, the available pressure work across the expansion fan is decreased. Around the shock incidence location marked by the pink ellipse in Fig. 13(d), which is close to the flame stabilization point, the pressure work fraction η^q is relatively higher than its surrounding. These results illustrate the importance of including the pressure work term in MMC-LES modeling of supersonic flames with shock interactions.

Figure 14 shows the time evolutions of the flame lift-off distances in cases 3 and 3a. The flame lift-off distance d_{lift} is identified as the streamwise distance between the strut base (i.e., $x = 109$ mm) and the flame base [identified as in Fig. 11(a)]. The mean lift-off distances are quite similar at 28.8 mm and 29.6 mm for cases 3 and 3a, respectively, and the flame base sits near the intersection of the incident shocks at $x \approx 140$ mm and inside the recirculation zone that is about 40 mm long. Interestingly, the oscillation of d_{lift} with time is much stronger when the Dp/Dt term is deactivated in case 3a. The pressure work contributes nearly one-fifth of the enthalpy at the shock front [see Fig. 13(d)], and without this effect, the flame stabilization is somewhat weaker and the flame base location is more variable.⁵⁰ In case 3a, the moving flame base nearly reaches the end of the recirculation zone at some instants, but it does not blow-off as it is supported by eddies of the hot product recirculating from downstream.

V. CONCLUSIONS

Sparse MMC-LES is extended to the supersonic combustion regime for the first time and validated against the data for a model combustor. A new compressible form of MMC-LES is developed, which specifically includes pressure work and viscous heating effects although the latter is negligibly small and can be neglected for the studied flow conditions. Incorporation of the sophisticated MMC closure for supersonic combustion including subgrid fluctuations but with fewer particles required than LES cells distinguishes the present work from previous MMC modeling of subsonic flows and quasi-laminar chemistry modeling of supersonic flows. The implementation involves a coupling of an Eulerian density-based

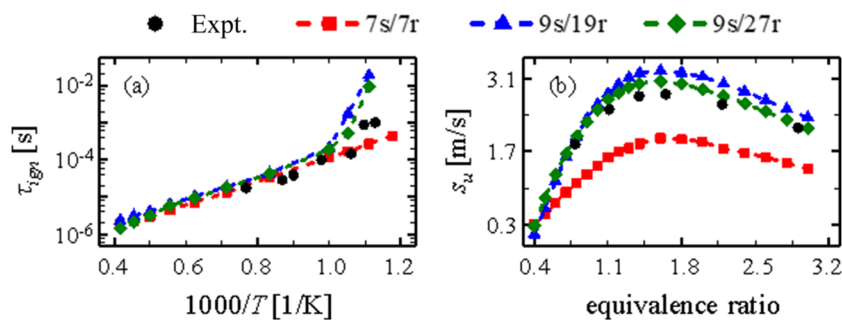


FIG. 15. Comparisons of (a) ignition delay time, τ_{ign} , and (b) laminar flame speed, s_u , for different hydrogen mechanisms (9s/27r,⁶⁹ 9s/19r,⁷⁴ and 7s/7r⁷⁵) with the experimental data.^{70,71}

Kurganov, Noelle, and Petrova scheme for filtered mass, momentum, and reference mixture fraction, which is suitable for flows with sharp discontinuities, and a stochastic Lagrangian scheme for the subfilter FDF of species and standardized enthalpy. Consistency between the two sub-schemes is achieved through additional Eulerian equations for equivalent composition and equivalent sensible enthalpy, which are coupled to the Lagrangian scheme via conditional source terms. The sensitivity of the results to variations in the sparse particle distribution over a range of 1L/10E to 1L/3E (representing a more than three times increase in the total particle number and associated computational expense) is investigated for the reacting flow cases and found to be negligible for velocity, pressure, temperature, and reactive species fields. The results of MMC-LES show good overall agreement with experimental data in terms of time-averaged quantities (axial velocity, temperature, and wall pressure) and second-order moments (root-mean-square fluctuation of axial velocity) at different streamwise locations and centerlines for both non-reacting and reacting flows. The numerical schlieren images also show close resemblance to their experimental counterparts including the spatial distribution of shocks, expansion fans, and recirculation zones. The pressure work term that is included in the stochastic differential equations is shown to have a significant role in predicting the unsteady behaviors of the flame base.

ACKNOWLEDGMENTS

This work was financially supported by the NUS (Grant No. R-265-000-604-133) and the USyd-NUS Partnership Collaboration Award. The simulations use ASPIRE 1 Cluster from the National Supercomputing Centre, Singapore (<https://www.nsc.sg/>).

APPENDIX: COMPARISON OF HYDROGEN MECHANISMS

The detailed mechanism for hydrogen/air combustion with 9 species/27 reactions⁶⁹ (9s/27r) used in this study is validated with the experimental data^{70,71} in terms of ignition delay time and laminar flame speed. Two additional mechanisms that are widely used for hydrogen/air combustion are also compared. They are Jachimowski's 9 species/19 reactions skeletal mechanism (9s/19r)⁷⁴ and Eklund's 7 species/7 reactions reduced mechanism (7s/7r).⁷⁵ Figure 15 shows the comparisons of ignition delay time (τ_{ign}) and laminar flame speed (s_u) from all three mechanisms with experimental data. It is found that the 9s/27r mechanism used in this work shows

good accuracy in calculating ignition delay time and laminar flame speed in a wide range, i.e., a temperature of 830 K–2500 K and an equivalence ratio of 0.4–3.2.

DATA AVAILABILITY

The data that support the findings of this study are available from the corresponding author upon reasonable request.

REFERENCES

- J. Urzay, "Supersonic combustion in air-breathing propulsion systems for hypersonic flight," *Annu. Rev. Fluid Mech.* **50**, 593–627 (2018).
- R. K. Seleznev, S. T. Surzhikov, and J. S. Shang, "A review of the scramjet experimental data base," *Prog. Aerosp. Sci.* **106**, 43–70 (2019).
- E. D. Gonzalez-Juez, A. R. Kerstein, R. Ranjan, and S. Menon, "Advances and challenges in modeling high-speed turbulent combustion in propulsion systems," *Prog. Energy Combust. Sci.* **60**, 26–67 (2017).
- Y. Moule, V. Sabelnikov, and A. Mura, "Highly resolved numerical simulation of combustion in supersonic hydrogen-air coflowing jets," *Combust. Flame* **161**, 2647–2668 (2014).
- L. Bouheraoua, P. Domingo, and G. Ribert, "Large-eddy simulation of a supersonic lifted jet flame: Analysis of the turbulent flame base," *Combust. Flame* **179**, 199–218 (2017).
- A. Saghaian, V. E. Terrapon, and H. Pitsch, "An efficient flamelet-based combustion model for compressible flows," *Combust. Flame* **162**, 652–667 (2015).
- G. V. Candler, N. Cymbalist, and P. E. Dimotakis, "Wall-modeled large-eddy simulation of autoignition-dominated supersonic combustion," *AIAA J.* **55**, 2410–2423 (2017).
- C. Liu, J. Yu, Z. Wang, M. Sun, H. Wang, and H. Grosshans, "Characteristics of hydrogen jet combustion in a high-enthalpy supersonic crossflow," *Phys. Fluids* **31**, 046105 (2019).
- K. Wu, P. Zhang, W. Yao, and X. Fan, "Computational realization of multiple flame stabilization modes in DLR strut-injection hydrogen supersonic combustor," *Proc. Combust. Inst.* **37**, 3685–3692 (2019).
- A. Vincent-Randonnier, V. Sabelnikov, A. Ristori, N. Zettervall, and C. Fureby, "An experimental and computational study of hydrogen-air combustion in the LAPCAT II supersonic combustor," *Proc. Combust. Inst.* **37**, 3703–3711 (2019).
- T. Hiejima and T. Oda, "Shockwave effects on supersonic combustion using hypermixer struts," *Phys. Fluids* **32**, 016104 (2020).
- Y. Liu, W. Zhou, Y. Yang, Z. Liu, and J. Wang, "Numerical study on the instabilities in H₂-air rotating detonation engines," *Phys. Fluids* **30**, 046106 (2018).
- Y. Fang, Y. Zhang, X. Deng, and H. Teng, "Structure of wedge-induced oblique detonation in acetylene-oxygen-argon mixtures," *Phys. Fluids* **31**, 026108 (2019).
- J. A. Fulton, J. R. Edwards, A. Cutler, J. McDaniel, and C. Goynes, "Turbulence/chemistry interactions in a ramp-stabilized supersonic hydrogen-air diffusion flame," *Combust. Flame* **174**, 152–165 (2016).

- ¹⁵F. A. Jaber, P. J. Colucci, S. James, P. Givi, and S. B. Pope, "Filtered mass density function for large-eddy simulation of turbulent reacting flows," *J. Fluid Mech.* **401**, 85–121 (1999).
- ¹⁶N. Peters, "Laminar flamelet concepts in turbulent combustion," *Symp. Combust.* **21**, 1231–1250 (1988).
- ¹⁷A. Y. Klimenko and R. W. Bilger, "Conditional moment closure for turbulent combustion," *Prog. Energy Combust. Sci.* **25**, 595–687 (1999).
- ¹⁸S. B. Pope, "PDF methods for turbulent reactive flows," *Prog. Energy Combust. Sci.* **11**, 119–192 (1985).
- ¹⁹L. Wang, H. Pitsch, K. Yamamoto, and A. Orii, "An efficient approach of unsteady flamelet modeling of a cross-flow-jet combustion system using LES," *Combust. Theory Modell.* **15**, 849–862 (2011).
- ²⁰D. Messig, F. Hunger, J. Keller, and C. Hasse, "Evaluation of radiation modeling approaches for non-premixed flamelets considering a laminar methane air flame," *Combust. Flame* **160**, 251–264 (2013).
- ²¹A. Scholtissek, F. Dietzsch, M. Gauding, and C. Hasse, "In situ tracking of mixture fraction gradient trajectories and unsteady flamelet analysis in turbulent non-premixed combustion," *Combust. Flame* **175**, 243–258 (2017).
- ²²F. Proch and A. M. Kempf, "Modeling heat loss effects in the large eddy simulation of a model gas turbine combustor with premixed flamelet generated manifolds," *Proc. Combust. Inst.* **35**, 3337–3345 (2015).
- ²³S. Mohamadnejad, P. Vena, S. Yun, and S. Kheirkhah, "Internal structure of hydrogen-enriched methane-air turbulent premixed flames: Flamelet and non-flamelet behavior," *Combust. Flame* **208**, 139–157 (2019).
- ²⁴A. Scholtissek, P. Domingo, L. Vervisch, and C. Hasse, "A self-contained composition space solution method for strained and curved premixed flamelets," *Combust. Flame* **207**, 342–355 (2019).
- ²⁵X. Wen, H. Wang, Y. Luo, K. Luo, and J. Fan, "Evaluation of flamelet/progress variable model for laminar pulverized coal combustion," *Phys. Fluids* **29**, 083607 (2017).
- ²⁶Y. Luo, X. Wen, H. Wang, K. Luo, and J. Fan, "Evaluation of different flamelet tabulation methods for laminar spray combustion," *Phys. Fluids* **30**, 053603 (2018).
- ²⁷F. Ladeinde, Z. Lou, and W. Li, "The effects of pressure treatment on the flamelet modeling of supersonic combustion," *Combust. Flame* **204**, 414–429 (2019).
- ²⁸M. Picciani, "Supersonic combustion modeling using the conditional moment closure approach," M.Sc. thesis, Cranfield University, 2014.
- ²⁹H. Möbus, P. Gerlinger, and D. Brüggemann, "Scalar and joint scalar-velocity-frequency Monte Carlo PDF simulation of supersonic combustion," *Combust. Flame* **132**, 3–24 (2003).
- ³⁰H. Koo, P. Donde, and V. Raman, "A quadrature-based LES/transported probability density function approach for modeling supersonic combustion," *Proc. Combust. Inst.* **33**, 2203–2210 (2011).
- ³¹S. K. Ghai, S. De, and A. Kronenburg, "Numerical simulations of turbulent lifted jet diffusion flames in a vitiated coflow using the stochastic multiple mapping conditioning approach," *Proc. Combust. Inst.* **37**, 2199–2206 (2019).
- ³²L. Zhang, J. Liang, M. Sun, H. Wang, and Y. Yang, "An energy-consistency-preserving large eddy simulation-scalar filtered mass density function (LES-SFMD) method for high-speed flows," *Combust. Theory Modell.* **22**, 1–37 (2018).
- ³³Y. P. De Almeida and S. Navarro-Martinez, "Large eddy simulation of a supersonic lifted flame using the Eulerian stochastic fields method," *Proc. Combust. Inst.* **37**, 3693–3701 (2019).
- ³⁴A. Y. Klimenko and S. B. Pope, "The modeling of turbulent reactive flows based on multiple mapping conditioning," *Phys. Fluids* **15**, 1907–1925 (2003).
- ³⁵M. J. Cleary and A. Y. Klimenko, "A detailed quantitative analysis of sparse-Lagrangian filtered density function simulations in constant and variable density reacting jet flows," *Phys. Fluids* **23**, 115102 (2011).
- ³⁶S. Subramaniam and S. B. Pope, "A mixing model for turbulent reactive flows based on Euclidean minimum spanning trees," *Combust. Flame* **115**, 487–514 (1998).
- ³⁷M. J. Cleary, A. Y. Klimenko, J. Janicka, and M. Pfitzner, "A sparse-Lagrangian multiple mapping conditioning model for turbulent diffusion flames," *Proc. Combust. Inst.* **32**, 1499–1507 (2009).
- ³⁸Z. Huo, F. Salehi, S. Galindo-Lopez, M. J. Cleary, and A. R. Masri, "Sparse MMC-LES of a Sydney swirl flame," *Proc. Combust. Inst.* **37**, 2191–2198 (2019).
- ³⁹G. Neuber, F. Fuest, J. Kirchmann, A. Kronenburg, O. T. Stein, S. Galindo-Lopez, M. J. Cleary, R. S. Barlow, B. Coriton, J. H. Frank, and J. A. Sutton, "Sparse-Lagrangian MMC modelling of the Sandia DME flame series," *Combust. Flame* **208**, 110–121 (2019).
- ⁴⁰N. Khan, M. J. Cleary, O. T. Stein, and A. Kronenburg, "A two-phase MMC-LES model for turbulent spray flames," *Combust. Flame* **193**, 424–439 (2018).
- ⁴¹S. Vo, O. T. Stein, A. Kronenburg, and M. J. Cleary, "Assessment of mixing time scales for a sparse particle method," *Combust. Flame* **179**, 280–299 (2017).
- ⁴²S. Galindo-Lopez, F. Salehi, M. J. Cleary, A. R. Masri, G. Neuber, O. T. Stein, A. Kronenburg, A. Varna, E. R. Hawkes, B. Sundaram, A. Y. Klimenko, and Y. Ge, "A stochastic multiple mapping conditioning computational model in OpenFOAM for turbulent combustion," *Comput. Fluids* **172**, 410–425 (2018).
- ⁴³W. Waidmann, F. Alfi, M. Böhm, U. Brummund, W. Clauß, and M. Oschwald, "Supersonic combustion of hydrogen/air in a scramjet combustion chamber," *Space Technol.* **15**, 421–429 (1995).
- ⁴⁴S. Sammak, Z. Ren, and P. Givi, "Modeling and simulation of turbulent mixing and reaction," in *Modeling and Simulation of Turbulent Mixing and Reaction: For Power, Energy and Flight* (Springer, Singapore, 2020), pp. 181–200.
- ⁴⁵A. Yoshizawa and K. Horiuti, "A statistically-derived subgrid-scale kinetic energy model for the large-eddy simulation of turbulent flows," *J. Phys. Soc. Jpn.* **54**, 2834–2839 (1985).
- ⁴⁶H. Pitsch and H. Steiner, "Large-eddy simulation of a turbulent piloted methane/air diffusion flame (Sandia flame D)," *Phys. Fluids* **12**, 2541–2554 (2000).
- ⁴⁷A. S. Potturi and J. R. Edwards, "Hybrid large-eddy/Reynolds-averaged Navier-Stokes simulations of flow through a model scramjet," *AIAA J.* **52**, 1417–1429 (2014).
- ⁴⁸H. Wang, F. Shan, Y. Piao, L. Hou, and J. Niu, "IDDES simulation of hydrogen-fueled supersonic combustion using flamelet modeling," *Int. J. Hydrogen Energy* **40**, 683–691 (2015).
- ⁴⁹Z. Huang, G. He, F. Qin, and X. Wei, "Large eddy simulation of flame structure and combustion mode in a hydrogen fueled supersonic combustor," *Int. J. Hydrogen Energy* **40**, 9815–9824 (2015).
- ⁵⁰Z. Huang, G. He, S. Wang, F. Qin, X. Wei, and L. Shi, "Simulations of combustion oscillation and flame dynamics in a strut-based supersonic combustor," *Int. J. Hydrogen Energy* **42**, 8278–8287 (2017).
- ⁵¹K. Wu, P. Zhang, W. Yao, and X. Fan, "Numerical investigation on flame stabilization in DLR hydrogen supersonic combustor with strut injection," *Combust. Sci. Technol.* **189**, 2154–2179 (2017).
- ⁵²C. Gong, M. Jangi, X.-S. Bai, J.-H. Liang, and M.-B. Sun, "Large eddy simulation of hydrogen combustion in supersonic flows using an Eulerian stochastic fields method," *Int. J. Hydrogen Energy* **42**, 1264–1275 (2017).
- ⁵³Y. Zheng and C. Yan, "Numerical investigations on the impact of turbulent Prandtl number and Schmidt number on supersonic combustion," *Fluid Dyn. Mater. Process.* **16**, 637–650 (2020).
- ⁵⁴R. L. Curl, "Dispersed phase mixing: I. Theory and effects in simple reactors," *AIChE J.* **9**, 175–181 (1963).
- ⁵⁵F. Salehi, M. J. Cleary, A. R. Masri, Y. Ge, and A. Y. Klimenko, "Sparse-Lagrangian MMC simulations of an *n*-dodecane jet at engine-relevant conditions," *Proc. Combust. Inst.* **36**, 3577–3585 (2017).
- ⁵⁶C. J. Greenshields, H. G. Weller, L. Gasparini, and J. M. Reese, "Implementation of semi-discrete, non-staggered central schemes in a colocated, polyhedral, finite volume framework, for high-speed viscous flows," *Int. J. Numer. Methods Fluids* **63**, 1–21 (2010).
- ⁵⁷A. Kurganov, S. Noelle, and G. Petrova, "Semidiscrete central-upwind schemes for hyperbolic conservation laws and Hamilton-Jacobi equations," *SIAM J. Sci. Comput.* **23**, 707–740 (2001).
- ⁵⁸Z. Huang and H. Zhang, "Investigations of autoignition and propagation of supersonic ethylene flames stabilized by a cavity," *Appl. Energy* **265**, 114795 (2020).
- ⁵⁹H. Zhang, M. Zhao, and Z. Huang, "Large eddy simulation of turbulent supersonic hydrogen flames with OpenFOAM," *Fuel* **282**, 118812 (2020).

- ⁶⁰C. Cao, T. Ye, and M. Zhao, "Large eddy simulation of hydrogen/air scramjet combustion using tabulated thermo-chemistry approach," *Chin. J. Aeronaut.* **28**, 1316–1327 (2015).
- ⁶¹M. Zhao, T. Zhou, T. Ye, M. Zhu, and H. Zhang, "Large eddy simulation of reacting flow in a hydrogen jet into supersonic cross-flow combustor with an inlet compression ramp," *Int. J. Hydrogen Energy* **42**, 16782–16792 (2017).
- ⁶²W. Wu, Y. Piao, and H. Liu, "Analysis of flame stabilization mechanism in a hydrogen-fueled reacting wall-jet flame," *Int. J. Hydrogen Energy* **44**, 26609–26623 (2019).
- ⁶³H. Jasak, "Error analysis and estimation for the finite volume method with applications to fluid flows," Ph.D. thesis, Imperial College London, 1996.
- ⁶⁴P. E. Kloeden and E. Platen, *Numerical Solution of Stochastic Differential Equations* (Springer, 1992).
- ⁶⁵E. Hairer and G. Wanner, *Solving Ordinary Differential Equations II: Stiff and Differential-Algebraic Problems*, 2nd ed. (Springer, 1996), Vol. 14.
- ⁶⁶J. H. Friedman, J. L. Bentley, and R. A. Finkel, "An algorithm for finding best matches in logarithmic expected time," *ACM Trans. Math. Software* **3**, 209–226 (1977).
- ⁶⁷J. R. Edwards, "Numerical simulations of shock/boundary layer interactions using time-dependent modeling techniques: A survey of recent results," *Prog. Aerosp. Sci.* **44**, 447–465 (2008).
- ⁶⁸S. B. Pope, "Ten questions concerning the large-eddy simulation of turbulent flows," *New J. Phys.* **6**, 35 (2004).
- ⁶⁹N. M. Marinov, C. K. Westbrook, and W. J. Pitz, "Detailed and global chemical kinetics model for hydrogen," *Transp. Phenom. Combust.* **1**, 118 (1996).
- ⁷⁰M. Slack and A. Grillo, "Investigation of hydrogen-air ignition sensitized by nitric oxide and by nitrogen dioxide," NASA Contract Report 2896, 1977.
- ⁷¹D. R. Dowdy, D. B. Smith, S. C. Taylor, and A. Williams, "The use of expanding spherical flames to determine burning velocities and stretch effects in hydrogen/air mixtures," *Symp. Combust.* **23**, 325–332 (1991).
- ⁷²C. Fureby, E. Fedina, and J. Tegnér, "A computational study of supersonic combustion behind a wedge-shaped flameholder," *Shock Waves* **24**, 41–50 (2014).
- ⁷³F. Génin and S. Menon, "Simulation of turbulent mixing behind a strut injector in supersonic flow," *AIAA J.* **48**, 526–539 (2010).
- ⁷⁴C. J. Jachimowski, "An analytical study of the hydrogen-air reaction mechanism with application to scramjet combustion," NASA Technical Paper 2791, 1988.
- ⁷⁵D. R. Eklund, S. D. Stouffer, and G. B. Northam, "Study of a supersonic combustor employing swept ramp fuel injectors," *J. Propul. Power* **13**, 697–704 (1997).